Volume 53 | Number 53 | 7 July 2017 | Pages 7103–7418

ChemComm

Chemical Communications

rsc.li/chemcomm

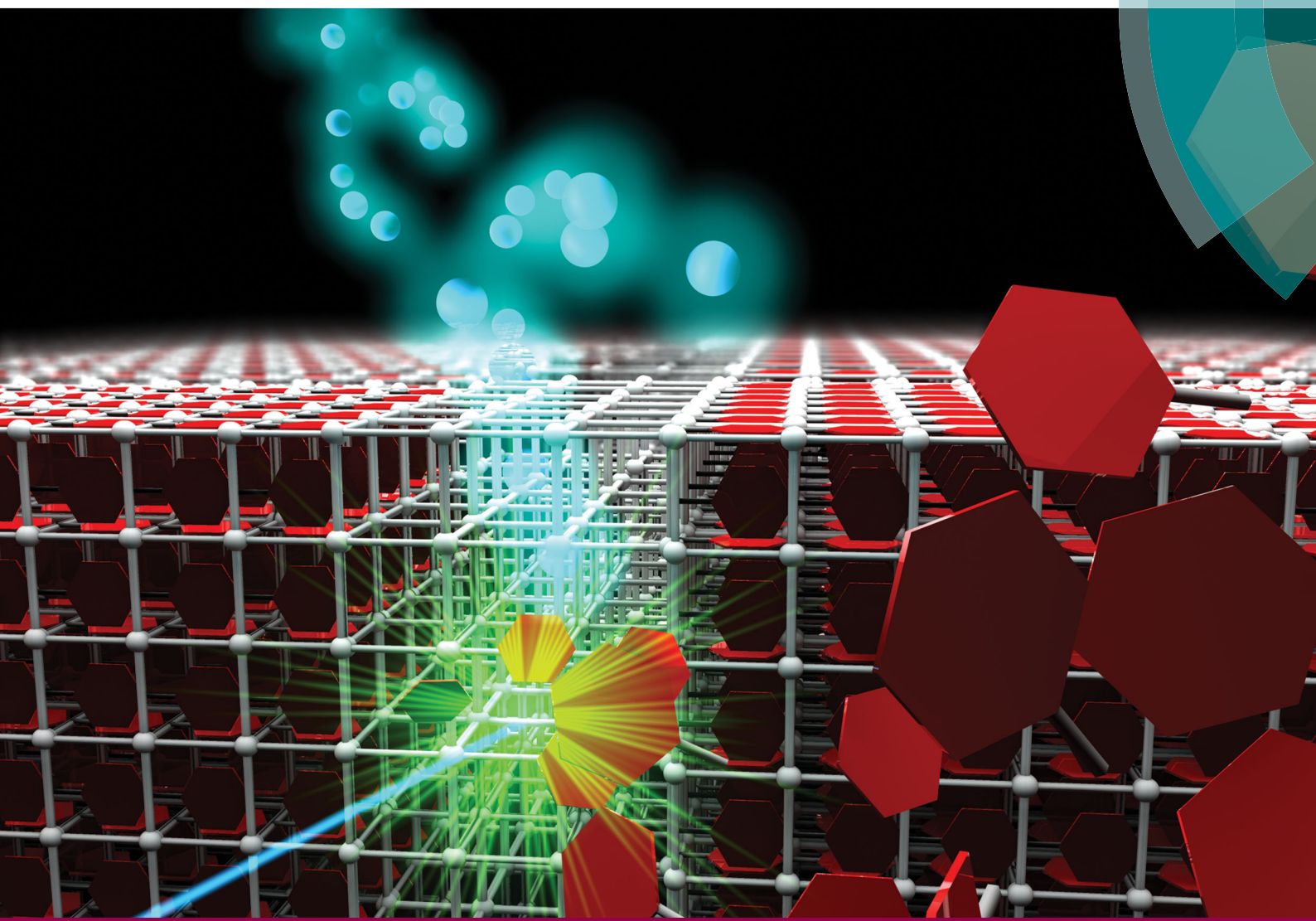

Themed issue: Emerging Investigators Issue 2017

ISSN 1359-7345

ROYAL SOCIETY OF CHEMISTRY

COMMUNICATION

R. Ameloot *et al.*

Photopatterning of fluorescent host–guest carriers through pore activation of metal–organic framework single crystals

ChemComm

COMMUNICATION

View Article Online
View Journal | View Issue

Cite this: *Chem. Commun.*, 2017, 53, 7222

Received 7th April 2017,
Accepted 25th April 2017

DOI: 10.1039/c7cc02709e

rsc.li/chemcomm

Photopatterning of fluorescent host–guest carriers through pore activation of metal–organic framework single crystals†

I. Stassen, [ab] I. Boldog, [a] C. Steuwe,[a] D. De Vos,[a] M. Roeffaers, [a] S. Furukawa [b] and R. Ameloot *[a]

Encoded fluorescent particles are fabricated through the selective uptake of dyes in photopatterned metal–organic framework single crystals. The concept is based on spatially controlled photochemical cleavage of pore-blocking pendant groups. Because of the crystalline and porous nature of the host, this approach enables guest uptake that is tunable and can be triggered though controlled irradiation.

Photopatterning is the process of transferring geometric patterns to photosensitive materials through spatially controlled irradiation. It can be used to introduce geometric complexity and anisotropy in materials beyond what more direct synthesis methods can achieve. A notable example of such optical encoding approaches is patterned photobleaching of dyed polymer microspheres to store information for readout by fluorescence imaging.[1] Photopatterning is also key in 'stop-flow' lithography for the reliable and high-throughput fabrication of functional polymer microstructures. Patterned and color-labeled structures produced by such methods are useful for application in anti-counterfeiting, multiplexed analytical chemistry or in rational design of metamaterials.[2,3] Although nanoporous materials could offer additional functionality in some of these applications, photofabrication and labeling routes remain unexplored for such solids.

Metal–organic frameworks (MOFs) are nanoporous materials built from multitopic organic linkers and metal-containing nodes.[4] These versatile and structurally tunable materials are emerging as platforms for the exploration of new scientific concepts at the micro-, meso- and nanoscale.[5,6] Through the organic linkers, photoresponsiveness can be incorporated in MOFs, *i.e.* frameworks that undergo chemical and structural transitions during irradiation with light.[7] For example, incorporating photoisomerizable azobenzene linkers enables photoswitchable host–guest interactions.[8–13] Another route is the photochemical cleavage of pendant groups.[14] For instance, postsynthetic deprotection of *o*-nitrobenzyl groups can be used to reveal chemical functionality that would interfere with the MOF crystallization (*e.g.* catechol),[15] to prevent framework interpenetration,[16] or to embed new functionalities through postsynthetic modification.[17]

The aforementioned postsynthetic photochemical modification strategies typically are performed on bulk quantities of a polycrystalline solid. By contrast, in our previous work we have shown the generation of metallic silver micro- and nanopatterns in single crystals of MOFs,[18] and related structures such as zeolites,[19] *via* spatially selective photochemical reduction of impregnated metal salts. Similarly, fluorescent encoding has recently been shown in MOF single crystals *via* the photo-induced oxidation of a pyridinium salt linker, resulting in enhanced emission.[20] However, as the previous methods depend on properties that are particular to the nanoporous host, tuning of the spectrophotometric properties of the encoded areas is not trivial.

Here we report a novel route for spatially controllable optical tailoring of MOF single crystals, *via* the inclusion of different fluorescent guests. Postsynthetic photochemical activation is utilized to control the accessibility of the pores and the infiltration of a range of fluorescent organic dyes to create distinct and bright fluorescent domains in predetermined locations. Moreover, we show that continuous tuning of the framework accessibility is possible through carefully controlling the irradiation time and degree of photodeprotection, and that the diameter of the fully activated MOF pores can be adjusted through isoreticular expansion.

The versatile and well-studied **IRMOF** series, first reported by Yaghi and co-workers,[21] was selected as the platform in this proof-of-concept study. Built from aromatic dicarboxylate linkers and Zn_4O nodes, **IRMOFs** are typically transparent in the visible range. Furthermore, previous studies showed that the pore size of **IRMOFs** is suitable for adsorption of some widely used fluorophores (*e.g.* structural analogs of fluorone).[22,23]

First, dicarboxylic acid linkers decorated with either one or two photocleavable *o*-nitrobenzyl pendant groups were synthesized

[a] *Centre for Surface Chemistry and Catalysis, KU Leuven - University of Leuven, Celestijnenlaan 200F, Leuven, 3001, Belgium. E-mail: rob.ameloot@kuleuven.be*
[b] *Institute for Integrated Cell-Material Sciences (WPI-iCeMS), Kyoto University, Yoshida, Sakyo-ku, Kyoto 606-8501, Japan*

† Electronic supplementary information (ESI) available: Detailed synthesis procedures for linkers and MOF monocrystals, experimental procedures, supporting experiments and figures (S1–S18). See DOI: 10.1039/c7cc02709e

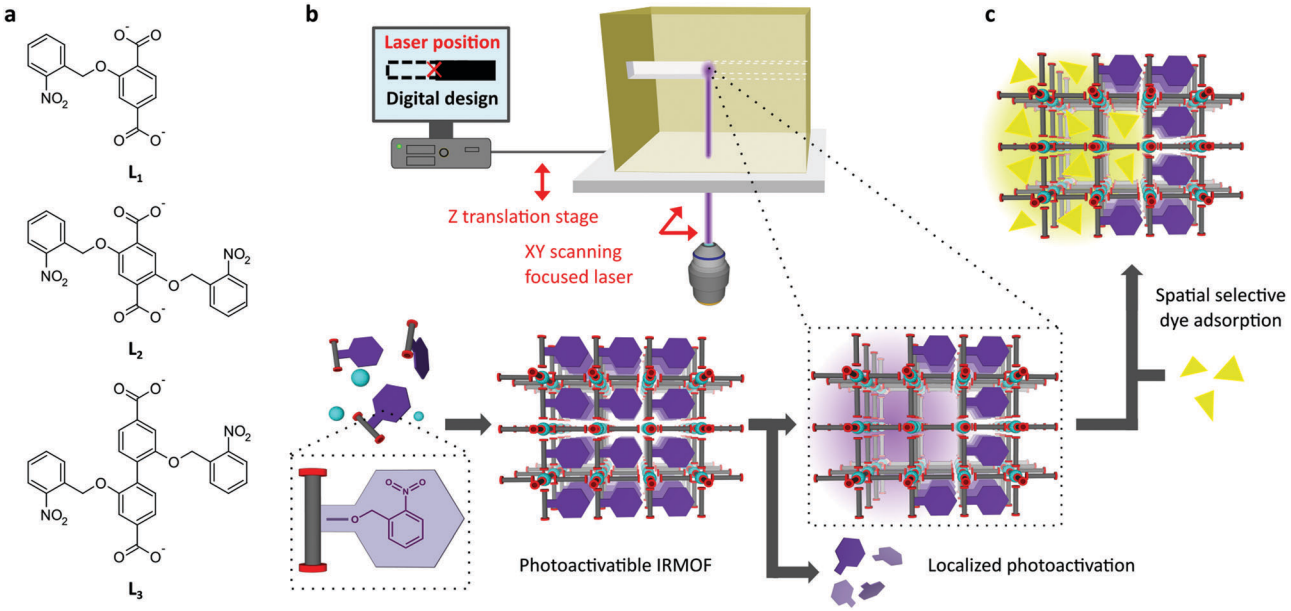

Fig. 1 Spatially selective photochemical activation of photoactivatable IRMOFs. (a) Chemical structure of the synthesized organic linkers decorated with pendant photocleavable *o*-nitrobenzyl groups. (b) Top: schematic representation of the utilized experimental setup: a focused continuous wave or pulsed laser scans the desired positions in the crystal. Bottom: scheme of the IRMOF synthesis using organic linkers and metal nodes and the subsequent patterned photochemical cleavage of the pendant groups by direct laser writing. (c) Spatially selective dye adsorption in the photoactivated area of the IRMOF enables the imaging of the nanoporous areas by confocal laser scanning microscopy (CLSM).

(Fig. 1a): 2-((2-nitrobenzyl)oxy)terephthalic acid (**L_1**), 2,5-di((2-nitrobenzyl)oxy)terephthalic acid (**L_2**) and 2,2′-bis-((2-nitrobenzyl)-oxy)-biphenyl-4,4′-dicarboxylic acid (**L_3**).‡ The photodeprotection rate of these linkers was monitored in solution by ^{1}H NMR during mild UV-A exposure and proved to be similar (Fig. S1–S3, ESI†).

Next, high-quality transparent crystals were synthesized based on **L_1** and confirmed to be analogs of **IRMOF-1**, *via* single crystal and power X-ray diffraction (Fig. S4, ESI†).§ Preliminary experiments indicated that the density of *o*-nitrobenzyl pendant groups in the **IRMOF-1-L_1** crystals was not high enough to exclude non-selective dye penetration. Although doubling the number of pendant groups seemed a straightforward strategy, we encountered difficulties in crystallizing high-quality **IRMOF-1** monocrystals using only **L_2**, probably due to steric hindrance. Hence, we optimized the synthesis of mixed-linker **IRMOF-1-L_1/L_2** crystals with a **L_1 : L_2** ratio of 58 : 42. This framework, containing approximately 4 pendant group per unit cell, displayed effective dye exclusion before photoactivation (Fig. S5, ESI†). Using our optimized protocol, faint yellow cubic crystals of 100–500 μm in size were obtained (Fig. S6 and S7, ESI†). The colored hue of **IRMOF-1-L_1/L_2** in comparison to colorless **IRMOF-1** can be explained by the incorporation of partially deprotected linkers that are formed through thermal reactions under the crystallization conditions. Nevertheless, ^{1}H NMR indicates that the vast majority (89%) of the pendant groups remains intact after incorporation in the framework (Fig. S8, ESI†).

Next we conducted a direct laser writing strategy, using a near-UV (405 nm) scanning laser microscope, to render certain areas within the **IRMOF-1-L_1/L_2** crystals guest-accessible (Fig. 1b). The uptake of fluorescent guests was subsequently used to visualize the accessible nanoporous regions in the crystals (Fig. 1c). Some opportunities that are enabled by this approach in combined particle patterning and color-labeling are illustrated in Fig. 2. The gradual darkening of the irradiated regions in the transmission image indicated the successful photodeprotection of the linkers. Importantly, the different emission and excitation characteristics of these host–guest particles are determined by the adsorbed dyes ($\lambda_{em\text{-}max}$ 500–700 nm, Fig. S9, ESI†). Strong accumulation of the guests in the accessible irradiated areas resulted in bright fluorescence, which is pronounced when compared to the emission of the diluted concentration (≈1 μM) solutions surrounding the crystals. Moreover, the color change of the photo-activated areas upon dye adsorption was clearly visible and remained relatively unchanged after soaking the crystals for several hours in neat solvent (Fig. S10, ESI†). In comparison to the guest-related signal, the autofluorescence of the framework was negligible as well (Fig. S11, ESI†).

The activation of well-defined zones *via* direct laser writing enables fabrication of anisotropic MOF crystals based on digital designs (*e.g.* the 'serpentine' shape in Fig. 2c). The state-of-the-art in asymmetric MOF particles includes a few demonstrations of polycrystalline assemblies,[24–26] but thus far no methods that allow anisotropic activation of pores within a single crystal.

In addition to spatial selectivity, direct laser writing offers control over the degree of photoreaction. Fig. 3 compares the emission intensity of zones activated at different UV exposure levels. By adjusting the laser exposure in the irradiated zone (0.8–6 μJ per pixel), the dye diffusion profile and plateau-level of emission change. At low exposure levels, the remaining *o*-nitrobenzyl pendant groups hamper dye diffusion and lower

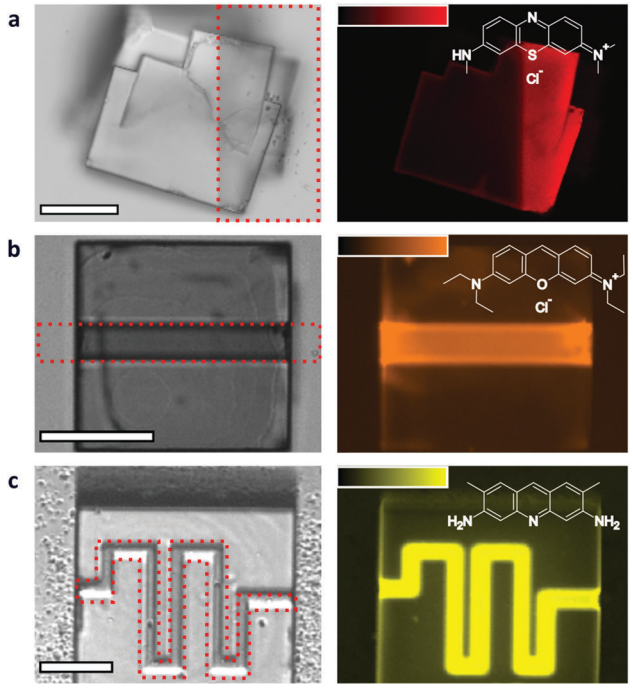

Fig. 2 Demonstration of rising degree of local anisotropy and spectrophotometric labelling through spatially selective photochemically activation of **IRMOF-1-L$_1$/L$_2$** carriers (5 μJ per pixel irradiation). Left: bright-field transmission microscopy image with red-dotted indicated area of photochemical activation. Right: CLSM image showing dye uptake in the activated area of the crystal (after 4 hours and at 25 μm height). (a) Asymmetric (Janus) architecture imaged at 650 nm (azure B; 10 μM; λ_{ex} = 635 nm). (b) Sandwich (2 : 1) architecture imaged at 600 nm (pyronin B; 100 nM; λ_{ex} = 559 nm). (c) Free shape 'serpentine' imaged at 530 nm (acridine Y; 100 μM; λ_{ex} = 488 nm). Relative intensity scales are shown in the top left of each CLSM image (0–4095 a.u.; 12 bit). Scale bars: 50 μm.

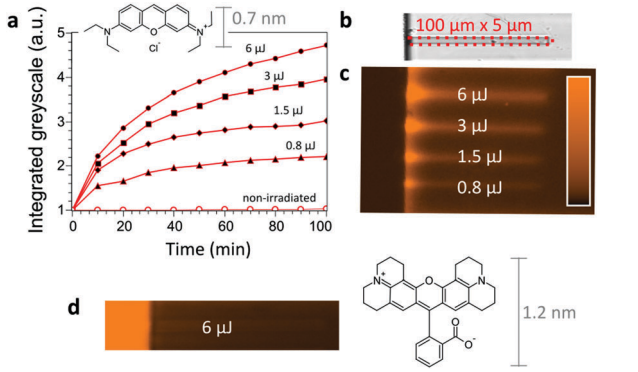

Fig. 3 Direct influence of the extent of photochemical activation on the porosity, monitored through the uptake of a pyronin B probe (100 nM; λ_{em} = 600 nm; λ_{ex} = 559 nm). Linear channels were made at 25 μm height using different irradiation times and the approximated energy—in μJ—per irradiated pixel is indicated. (a) Plot of integrated intensity (grey scale) of the irradiated zones in function of time. (b) Bright-field transmission microscopy image of an irradiated channel with red-dotted indication of the area of photochemical activation. (c) CLSM image showing uptake after immersing the crystal in 100 nM pyronin B for 90 minutes. (d) Reference experiment indicating intact crystallinity through size-exclusion of Rhodamine 101 (100 μM; λ_{em} = 600 nm; λ_{ex} = 559 nm). The relative intensity scale of the images is shown at the right (0–4095 a.u.; 12 bit).

the adsorption capacity. This strategy can therefore be used to control the fluorescence intensity of deprotected areas. Repeating this experiment with dyes too large to pass through the 0.80 nm pore aperture of the fully activated **IRMOF-1-L$_1$/L$_2$** framework confirmed that no uptake takes place in the irradiated area, even at dye concentrations as high as 100 μM (Fig. 3d). This molecular sieving effect confirms the intactness of the framework crystal lattice in the photochemically activated areas.

Naturally, the upper size limit of the probe is linked to the pore aperture of the MOF. Therefore, the concept can be extended to larger molecules through isoreticular expansion of the framework. Accordingly, single crystals were synthesized using the extended linker—**L$_3$** (Fig. 1a)—and confirmed to be analogs of IRMOF-10 (Fig. S12, ESI†). Notably, in this case dark orange to red crystals were obtained, which is consistent with the slightly higher observed deprotection rate of the incorporated linker (Fig. S13 and S14, ESI†). Nevertheless, a majority of the linkers (78%) contained both protecting groups after synthesis of the crystals (Fig. S15, ESI†).

The structure of **IRMOF-10-L$_3$** is characterized by a much wider pore aperture (1.25 nm) and accommodation of rather bulky phenyl-substituted fluorone dyes can be anticipated after activation (Fig. S16, ESI†). Indeed, in Fig. S17 (ESI†) spatially selective uptake of Rhodamine 101 in **IRMOF-10-L$_3$** is shown at distinct heights correlating with the positioning of the focal plane after writing of the linear channels with a near-infrared pulsed laser. While the approximate average decoration of 5 pendant groups per unit cell in **IRMOF-10-L$_3$** appears to be adequate to significantly hamper diffusion of similar bulky dyes (in the time scale of multiple hours), a higher density of such groups, either more bulky groups (*e.g.* *p*/*m*-substituted *o*-nitrobenzyl), will be needed to fully block more compact molecules from entering the non-irradiated areas.

Spatially selective photochemical activation can also be utilized as a 'stackable' feature in the sense that it can be combined with other MOF functionalization strategies. For example, we prepared core–shell **IRMOF-1-L$_1$/L$_2$@IRMOF-1** carriers, by adjusting a previously reported protocol.[27] These structures displayed uptake of a dye in the non-functionalized IRMOF-1 core that was directly conditioned by irradiation of the **IRMOF-1-L$_1$/L$_2$** shell (Fig. 4 and Fig. S18, ESI†).

Based on our findings we anticipate new strategies for rational design of crystalline molecular flasks,[28] intracrystalline diffusion studies,[29] or molecular separations.[22] Nevertheless, the moisture sensitivity of Zn_4O **IRMOFs** requires handling under solvated and humidity-free conditions. Amorphization and cracking of the monocrystals upon laser exposure was observed when such measures were not taken. Extending the concept to MOFs with enhanced ambient stability will make it more viable for other potential applications, *e.g.* in analytical biochemistry and *in vivo* labeling.

In conclusion, this study demonstrates a novel method for intracrystalline spatially selective activation of nanoporous MOFs. Using this method, accessibility of the pores to guest molecules can be gradually tuned, as was shown for organic fluorescent

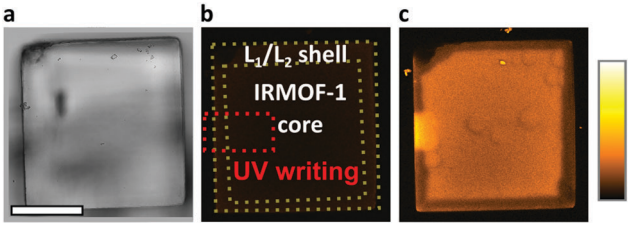

Fig. 4 Phototriggered pyronin B uptake by **IRMOF-1-L_1/L_2@IRMOF-1** core–shell carriers. (a) Bright-field transmission microscopy image of the crystal. (b) CLSM image of the crystal after 120 min soaking in pyronin B (100 nM; λ_{em} = 600 nm; λ_{ex} = 559 nm), with red-dotted indicated area of photochemical activation and the grey-dotted lines indicating the core and shell components of the assembly. (c) CLSM image of the crystal after UV irradiation and 120 min additional soaking in the unaltered dye solution. The relative intensity scale is shown at the right (0–4095 a.u.; 12 bit). Scale bar 100 μm.

tracers by CSLM. We envision that this method can lead to new breakthroughs in rational design of nanoporosity for molecular carriers and other miniaturized systems.

I. S. thanks the Research Foundation—Flanders (FWO) for a fellowship and travel grant (V425114N). The authors thank S. Verheyden for assistance in the experimental preparation of this work. FWO and the Japan Society for Promotion of Science (JSPS) are acknowledged for funding in the form of a cooperation project (VS03215N). The KU Leuven Cell Imaging Core (CIC) is acknowledged for their facilities. R. A. is grateful to KU Leuven for BOF-START funding STG/14/07BF.

Notes and references

‡ Experimental procedures and characterization can be found in the ESI.† A reported procedure for $\mathbf{L_1}$ was utilized to design and optimize similar synthesis procedures for $\mathbf{L_2}$ and $\mathbf{L_3}$.
§ Single crystal X-ray diffraction space group and unit cell dimension: $Pm\bar{3}m$; a = 12.983 Å and $P432$; a = 17.472 Å, respectively for our analogs of **IRMOF-1** and **IRMOF-10**.

1 K. Braeckmans, S. C. De Smedt, C. Roelant, M. Leblans, R. Pauwels and J. Demeester, *Nat. Mater.*, 2003, **2**, 169–173.
2 D. C. Pregibon, M. Toner and P. S. Doyle, *Science*, 2007, **315**, 1393–1396.
3 J. Lee, P. W. Bisso, R. L. Srinivas, J. J. Kim, A. J. Swiston and P. S. Doyle, *Nat. Mater.*, 2014, **13**, 524–529.
4 H. Furukawa, K. E. Cordova, M. O'Keeffe and O. M. Yaghi, *Science*, 2013, **341**, 1230444.
5 P. Falcaro, R. Ricco, C. M. Doherty, K. Liang, A. J. Hill and M. J. Styles, *Chem. Soc. Rev.*, 2014, **43**, 5513–5560.
6 R. Ricco, C. Pfeiffer, K. Sumida, C. J. Sumby, P. Falcaro, S. Furukawa, N. R. Champness and C. J. Doonan, *CrystEngComm*, 2016, **18**, 6532–6542.
7 C. L. Jones, A. J. Tansell and T. L. Easun, *J. Mater. Chem. A*, 2016, **4**, 6714–6723.
8 A. Modrow, D. Zargarani, R. Herges and N. Stock, *Dalton Trans.*, 2011, **40**, 4217–4222.
9 J. Park, D. Yuan, K. T. Pham, J.-R. Li, A. Yakovenko and H.-C. Zhou, *J. Am. Chem. Soc.*, 2012, **134**, 99–102.
10 R. Lyndon, K. Konstas, B. P. Ladewig, P. D. Southon, P. C. J. Kepert and M. R. Hill, *Angew. Chem., Int. Ed.*, 2013, **52**, 3695–3698.
11 R. D. Mukhopadhyay, V. K. Praveen and A. Ajayaghosh, *Mater. Horiz.*, 2014, **1**, 572–576.
12 L. Heinke, M. Cakici, M. Dommaschk, S. Grosjean, R. Herges, S. Bräse and C. Wöll, *ACS Nano*, 2014, **8**, 1463–1467.
13 Z. Wang, L. Heinke, J. Jelic, M. Cakici, M. Dommaschk, R. J. Maurer, H. Oberhofer, S. Grosjean, R. Herges, S. Bräse, K. Reuter and C. Wöll, *Phys. Chem. Chem. Phys.*, 2015, **17**, 14582–14587.
14 S. Diring, D. O. Wang, C. Kim, M. Kondo, Y. Chen, S. Kitagawa, K. Kamei and S. Furukawa, *Nat. Commun.*, 2013, **4**, 2684.
15 K. K. Tanabe, C. A. Allen and S. M. Cohen, *Angew. Chem., Int. Ed.*, 2010, **49**, 9730–9733.
16 R. K. Deshpande, G. I. N. Waterhouse, G. B. Jameson and S. G. Telfer, *Chem. Commun.*, 2012, **48**, 1574–1576.
17 C. A. Allen and S. M. Cohen, *J. Mater. Chem.*, 2012, **22**, 10188.
18 R. Ameloot, M. B. J. Roeffaers, G. De Cremer, F. Vermoortele, J. Hofkens, B. F. Sels and D. E. De Vos, *Adv. Mater.*, 2011, **23**, 1788–1791.
19 G. De Cremer, B. F. Sels, J. Hotta, M. B. J. Roeffaers, E. Bartholomeeusen, E. Coutiño-Gonzalez, V. Valtchev, D. E. De Vos, T. Vosch and J. Hofkens, *Adv. Mater.*, 2010, **22**, 957–960.
20 J. Yu, Y. Cui, C.-D. Wu, Y. Yang, B. Chen and G. Qian, *J. Am. Chem. Soc.*, 2015, **137**, 4026–4029.
21 M. Eddaoudi, J. Kim, N. Rosi, D. Vodak, J. Wachter, J. Kim, N. Rosi, D. Vodak, J. Wachter, M. O'Keeffe and O. Yaghi, *Science*, 2002, **295**, 469–472.
22 S. Han, Y. Wei, C. Valente, I. Lagzi, J. J. Gassensmith, A. Coskun, J. F. Stoddart and B. A. Grzybowski, *J. Am. Chem. Soc.*, 2010, **132**, 16358–16361.
23 S. M. Shin, M. S. Lee, J. H. Han and N. Jeong, *Chem. Commun.*, 2014, **50**, 289–291.
24 S. Yadnum, J. Roche, E. Lebraud, P. Négrier, P. Garrigue, D. Bradshaw, C. Warakulwit, J. Limtrakul and A. Kuhn, *Angew. Chem., Int. Ed.*, 2014, **53**, 4001–4005.
25 T.-H. Park, K. J. Lee, S. Hwang, J. Yoon, C. Woell and J. Lahann, *Adv. Mater.*, 2014, **26**, 2883–2888.
26 A. Ayala, C. Carbonell, I. Imaz and D. Maspoch, *Chem. Commun.*, 2016, **52**, 5096–5099.
27 K. Koh, A. G. Wong-Foy and A. J. Matzger, *Chem. Commun.*, 2009, 6162.
28 Y. Inokuma, M. Kawano and M. Fujita, *Nat. Chem.*, 2011, **3**, 349–358.
29 T. Titze, A. Lauerer, L. Heinke, C. Chmelik, N. E. R. Zimmermann, F. J. Keil, D. M. Ruthven and J. Kärger, *Angew. Chem., Int. Ed.*, 2015, **54**, 14580–14583.